Research in Astronomy and Astrophysics, 23:085013 (14pp), 2023 August https://doi.org/10.1088/1674-4527/acd73c


# IP Lyn: A Totally Eclipsing Contact Binary with an Extremely Low Mass Ratio

Zi-Xuan Yin[1], Zi-Bin Meng[1], Pei-Ru Wu[1], Xu-Dong Zhang[2], Yun-Xia Yu[1,3], Ke Hu[1,3], and Fu-Yuan Xiang[1,3]
[1] Key Laboratory of Star and Interstellar Medium, Xiangtan University, Xiangtan 411105, China; yu.sunny@126.com
[2] School of Physics and Electronic Science, Guizhou Normal University, Guiyang 550025, China
[3] Department of Physics, Xiangtan University, Xiangtan 411105, China
*Received 2023 March 20; revised 2023 May 8; accepted 2023 May 15; published 2023 July 10*

## Abstract

We present the first photometric and orbital period investigations for a neglected totally eclipsing contact binary IP Lyn. The photometric solutions derived from both ground-based and several surveys' observations suggest that it is a shallow contact binary with an extremely low mass ratio of 0.055. The weak asymmetry observed in our multiple band light curves can be interpreted as a result of an active cool spot on the primary. The absolute physical parameters were determined with the Gaia-distance-based method and checked by an empirical relation. Combining the eclipse timings collected from the literature and those derived from our and variable surveys' observations, we find that IP Lyn has been undergoing a secular orbital period increase for the past two decades, implying a mass transfer from the less massive secondary to the primary. By comparing the current parameters with the critical instability ones, we infer that IP Lyn is currently stable in spite of its relatively low mass ratio and orbital angular momentum. Finally, from a catalog of 117 extremely low mass ratio contact binaries, we find that their orbital angular momenta are significantly lower than those of the contact binaries with a relatively high mass ratio, suggesting they should be at the late evolutionary stage of a contact binary.

*Key words:* (stars:) binaries (including multiple): close – (stars:) binaries: eclipsing – stars: evolution – stars: individual (IP Lyn)

## 1. Introduction

Contact binaries, which are composed of two Roche-lobe filling stars embedded in a shared convective envelope (Ruciński 1967), are relatively common in our Galaxy. According to the estimates of Rucinski (2007), one in every 500 stars may be a contact binary. As an important part of the Galactic stellar population, they have been frequently observed and intensively investigated for about one century, and a comprehensive evolutionary sequence has been well developed. According to the evolutionary pathway outlined by Eggleton (2012), contact binaries originated from close detached binaries via the angular momentum loss brought on by magnetic braking and tidal friction. After undergoing a long geriatric contact stage, their evolution will come to an end in a merger of component stars. Although the fundamentals of binary evolution may be well understood, several scenarios involving the formation, evolution and outcomes are still elusive. Also, some extended issues, such as the mass-ratio lower limit (Rasio & Shapiro 1995; Li & Zhang 2006; Arbutina 2007, 2012; Yang & Qian 2015; Wadhwa et al. 2021a, 2021; Pešta & Pejcha 2023) and the orbital period cutoff (Rucinski 1992; Nefs et al. 2012; Davenport et al. 2013; Zhang et al. 2020), are still matters of controversy and debate. Perhaps these issues can be resolved by gradually accumulating the individually-studied samples.

Theoretical studies suggested that a contact binary will encounter tidal instability (i.e., Darwin's instability, Darwin 1908) and merge fast into a single, rapidly rotating object when the orbital angular momentum is less than three times the spin angular momentum (Counselman 1973; Webbink 1976; Hut 1980). Theoretically, the criterion of instability is also associated with the lower limit on mass ratio (Rasio & Shapiro 1995; Qian et al. 2006; Yang & Qian 2015). When the mass ratio falls below a theoretical threshold, Darwin's instability will be triggered and drive a contact binary to merge into a single star. In observation, V1309 Sco provided a prototype for a binary merger. From the archived photometric data on this object in the Optical Gravitational Lensing Experiment (OGLE) project, the progenitor of V1309 Sco was confirmed to be a contact binary with an extremely low mass ratio ($q = 0.094$) (Tylenda et al. 2011; Zhu et al. 2016; Mason & Shore 2022). Thus, the extremely low mass ratio contact binaries (ELMRCBs) have been considered as the most plausible progenitors of mergers and intensively investigated for the past two decades. Currently, a large number of ELMRCBs have been identified (Yang & Qian 2015; Christopoulou et al. 2022; Kobulnicky et al. 2022; Li et al.

**Table 1**
Parameters of Target Star, Comparison Star and Check Star

| Object | $\alpha_{2000}$ | $\delta_{2000}$ | $B$(mag) | $V$(mag) | Period | Parallax(mas) |
|---|---|---|---|---|---|---|
| IP Lyn | $08^h02^m23\overset{s}{.}474$ | $51°46'45\overset{''}{.}066$ | 12.840 | 12.535 | 0.489 115 | $1.019 \pm 0.059$ |
| TYC 3414-2428-1 | $08^h02^m40\overset{s}{.}186$ | $51°47'39\overset{''}{.}966$ | 12.523 | 12.216 | ⋯ | $1.149 \pm 0.042$ |
| APASS 56748689 | $08^h02^m50\overset{s}{.}985$ | $51°47'06\overset{''}{.}911$ | 13.683 | 13.155 | ⋯ | $0.979 \pm 0.032$ |

2022). Among them, some systems, such as V1187 Her ($q = 0.044$, Caton et al. 2019), VSX J082700.8+462850 ($q = 0.055$, Li et al. 2021a), KIC 4244929 ($q = 0.059$, Śenavcı et al. 2016, ASAS J083241+2332.4 ($q = 0.067$, Sriram et al. 2016) and V857 Her ($q = 0.065$, Qian et al. 2005), have mass ratios that are even lower than the typical limit ($0.07 \sim 0.09$) predicted by several previous theoretical models (Rasio & Shapiro 1995; Li & Zhang 2006; Arbutina 2007, 2012). These systems challenge the associated theoretical models. Subsequently, Jiang et al. (2010) argued that the minimum mass ratio can be dropped down to 0.05 by taking into account the primary's mass and structure. Also, based on the statistical analysis of 46 low mass ratio contact binaries, Yang & Qian (2015) estimated a lowest mass ratio of 0.044. Recently, with Bayesian inference, Pešta & Pejcha (2023) derived the mass-ratio distribution of contact binaries and obtained a mass ratio lower limit of 0.030. Because the mass ratios of ELMRCBs are very close to or even lower than the theoretical limit, the search and analyses for such systems are very helpful for refining the theoretical models and identifying the underlying progenitors of the merger.

In this work, we present the first photometric and orbital period investigation for a neglected contact binary IP Lyn. Its variable nature was discovered by the Northern Sky Variability Survey (NSVS, Woźniak et al. 2004). Subsequently, it was scanned by the Super Wide Angle Search for Planets (SuperWASP[4], Butters et al. 2010) project. According to the photometric observations of these surveys, IP Lyn was classified as a variable with EW-type light curves (Khruslov 2013). At the same time, Khruslov (2013) determined the preliminary elements, such as the light curve amplitude and orbital periods. The All-Sky Automated Survey for Supernovae (ASAS-SN[5], Shappee et al. 2014; Kochanek et al. 2017; Jayasinghe et al. 2018), the Zwicky Transient Facility (ZTF[6], Bellm et al. 2019) and the Gaia mission[7] (Gaia Collaboration et al. 2019, 2020) also scanned the target, but these photometric observations were discontinuous, single-band or wide-band. On the observational side and considering the spectrum, this system was scanned by the Large Sky Area Multi-Object Fiber Spectroscopic Telescope (LAMOST,[8] Luo et al. 2015) spectral survey, and its spectroscopic elements were clearly revealed. Despite the wealth of observational data from various surveys, a systematic investigation involving the photometric nature and evolutionary status of this system is yet missing. Here we perform the multi-band CCD photometric observations of IP Lyn. Together with those survey data, we attempt to uncover its photometric nature, orbital period behavior and evolutionary status.

## 2. Observations

IP Lyn was observed on 2018 January 21 with the 85 cm reflecting telescope at the Xinglong Station of National Astronomical Observatories, Chinese Academy of Sciences (NAOC). The telescope was equipped with a Cassegrain-focus multi-band CCD photometer, which has $2048 \times 2048$ square pixels. During our observations, Johnson Cousins $BVR$ filters and an Andor DZ936 PI2048 CCD photometric system were adopted. We obtained a total of 2465 images (818 in $B$ band, 824 in $V$ band and 823 in $R$ bands). All images were then reduced into photometric data using the aperture photometry package from the `Image Reduction and Analysis Facility` (`IRAF`[9]). In the fields of view, we selected two single stars as the comparison and check stars, respectively. Because they are very close to the target IP Lyn, the extinction correction was not made. From the International Variable Star Index and the Set of Identifications, Measurements and Bibliography for Astronomical Data (SIMBAD) database, we collected their basic information in Table 1. The photometric data are presented as the magnitude differences between the target and comparison in Table 2.

The phase-folded light curves are depicted in Figure 1, which show a typical EW-type luminosity variation. Combining the EW-type luminosity variation with the relatively short orbital period, we may infer that IP Lyn should be a contact binary. Although the photometric data exhibit a relatively large scatter, a slight asymmetry and a wide, flat bottom around the 0.5 phase can be found by visual inspection. Because the flat bottom corresponding to the secondary eclipse is significantly

4 https://wasp.cerit-sc.cz/form
5 https://asas-sn.osu.edu/
6 https://www.ztf.caltech.edu/
7 https://www.cosmos.esa.int/gaia
8 http://www.lamost.org/public/
9 `IRAF` is distributed by the National Optical Astronomy Observatory (NOAO), which is operated by the Association of Universities for Research in Astronomy, Inc., under cooperative agreement with the National Science Foundation (NSF). http://iraf.noao.edu/

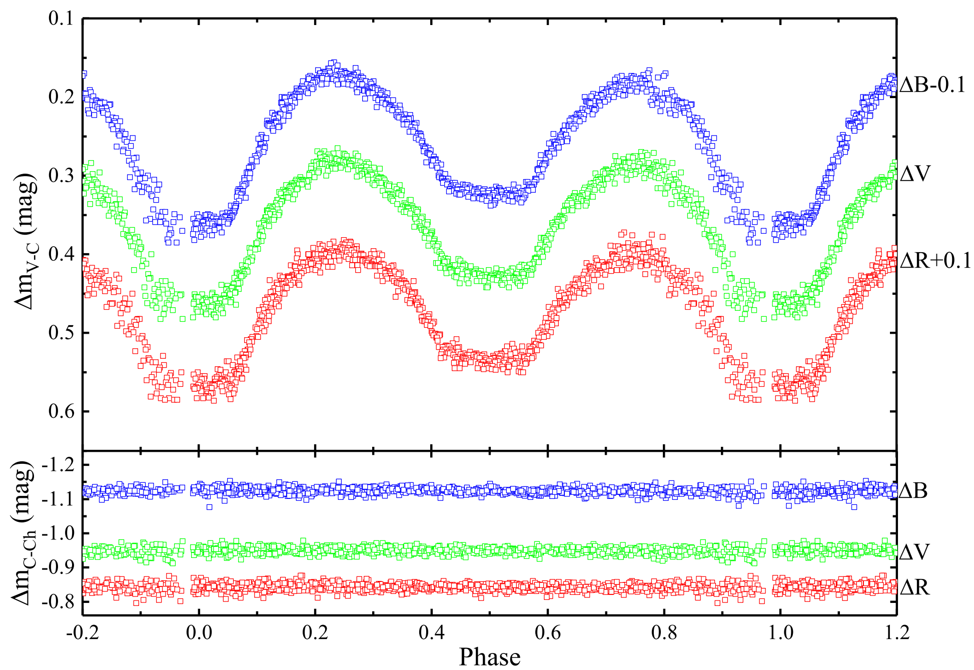


**Figure 1.** *BVR*-band photometric light curves of IP Lyn. The corresponding magnitude differences between the comparison and check stars are displayed in the bottom panel.

**Table 2**
*BVR*-Band Photometric Data of IP Lyn

| *B* band | | | *V* band | | | *R* band | | |
|---|---|---|---|---|---|---|---|---|
| JD(Hel.) | Phase | Δ*m* | JD(Hel.) | Phase | Δ*m* | JD(Hel.) | Phase | Δ*m* |
| 2458141.96902 | 0.9898 | 0.474 | 2 458 141.969 15 | 0.9901 | 0.480 | 2 458 141.969 27 | 0.9903 | 0.468 |
| 2458141.96945 | 0.9907 | 0.455 | 2 458 141.969 57 | 0.9910 | 0.463 | 2 458 141.969 69 | 0.9912 | 0.453 |
| 2458141.96987 | 0.9916 | 0.468 | 2 458 141.970 00 | 0.9918 | 0.461 | 2 458 141.970 11 | 0.9921 | 0.471 |
| 2458141.97029 | 0.9924 | 0.482 | 2 458 141.970 43 | 0.9927 | 0.451 | 2 458 141.970 54 | 0.9929 | 0.471 |
| 2458141.97098 | 0.9938 | 0.460 | 2 458 141.971 14 | 0.9942 | 0.454 | 2 458 141.971 26 | 0.9944 | 0.458 |
| 2458141.97147 | 0.9948 | 0.468 | 2 458 141.971 63 | 0.9952 | 0.454 | 2 458 141.971 75 | 0.9954 | 0.469 |
| 2458141.97195 | 0.0165 | 0.461 | 2 458 141.972 12 | 0.9962 | 0.470 | 2 458 141.972 22 | 0.9964 | 0.483 |
| 2458141.97243 | 0.9968 | 0.449 | 2 458 141.972 59 | 0.9971 | 0.460 | 2 458 141.972 71 | 0.0187 | 0.470 |
| ... | ... | ... | ... | ... | ... | ... | ... | ... |
| 2458142.44714 | 0.9674 | 0.453 | 2 458 142.439 44 | 0.9516 | 0.439 | 2 458 142.439 68 | 0.9521 | 0.451 |
| 2458142.44910 | 0.0181 | 0.470 | 2 458 142.440 30 | 0.9534 | 0.447 | 2 458 142.441 38 | 0.9556 | 0.472 |
| | | | 2 458 142.441 15 | 0.9551 | 0.471 | 2 458 142.442 23 | 0.9416 | 0.485 |
| | | | 2 458 142.443 70 | 0.9603 | 0.456 | 2 458 142.443 94 | 0.9608 | 0.460 |
| | | | 2 458 142.444 56 | 0.0527 | 0.451 | 2 458 142.444 79 | 0.9573 | 0.485 |
| | | | 2 458 142.447 44 | 0.9680 | 0.452 | 2 458 142.447 65 | 0.9684 | 0.465 |
| | | | 2 458 142.448 27 | 0.0537 | 0.451 | 2 458 142.448 50 | 0.9701 | 0.450 |
| | | | 2 458 142.449 36 | 0.9719 | 0.482 | | | |

**Note.** The full data set of Table 2 is compiled as a supplementary file (mst1-mrt.txt) in machine-readable format. Here a portion is presented for guidance regarding its form and content.

wider than that of the primary eclipse, IP Lyn should be an A-subtype and a totally eclipsing contact binary. In addition, the smaller amplitude and wide, flat bottom indicate that it could be an ELMRCB (Rucinski et al. 2001).

The LAMOST spectral survey provided three low-resolution spectral observations for IP Lyn, and the atmospheric surface parameters, such as effective temperature, surface gravity, metallicity, etc., have been extrapolated using the LAMOST Stellar Parameter Pipeline (Luo et al. 2015). These spectral elements and observation phases are summarized in Table 3. As should be noted, the observation time for the second spectrum completely corresponds to the total eclipse region

**Table 3**
Three Sets of Spectroscopic Elements for IP Lyn Extracted from LAMOST Spectra

| Obs. Data | Median HJD | Phase | Sp. Type | $T_{\rm eff}$ | $\log g$ | Fe/H | Rad. Velocity |
|---|---|---|---|---|---|---|---|
| 2013-1-8 | 2 456 301.1903 | 0.5381 | F3V | $6655 \pm 22$ | $4.166 \pm 0.031$ | $0.018 \pm 0.018$ | $-41.00 \pm 3.01$ |
| 2014-11-3 | 2 456 965.4003 | 0.5214 | F3V | $6675 \pm 12$ | $4.184 \pm 0.015$ | $0.035 \pm 0.007$ | $-46.24 \pm 2.12$ |
| 2016-2-20 | 2 457 439.1475 | 0.1019 | F3V | $6694 \pm 32$ | $4.155 \pm 0.043$ | $-0.001 \pm 0.025$ | $-52.87 \pm 4.77$ |

around 0.5 phase. This implies that the observed fluxes of this spectrum come fully from the primary's hemisphere. Thus, we will adopt the elements of the second spectrum as the primary's parameters in the following light curve analysis.

## 3. Orbital Period Investigations

Due to the discontinuous and low-precision photometric observations of the early surveys, the linear ephemerides of IP Lyn derived by Khruslov (2013), perhaps, are not very accurate. In order to determine the exact ephemeris and uncover possible period variations, we perform a careful search for the eclipse timings of the binary system and found one eclipse timing for IP Lyn. Based on the photometric data from several surveys, we calculated the phase-folded light curves according to the observational seasons, and determined 35 eclipse timings for IP Lyn with the method of Borkovits et al. (2015). From our observations, we derived two eclipse timings with the Kwee–van Woerden method (Kwee & van Woerden 1956). Together with those eclipse timings collected from the literature, a total of 38 data points are obtained and compiled in Table 4. With the linear ephemeris (Khruslov 2013)

$$\mathrm{Min.I} = \mathrm{HJD}2454501.473 + 0.489\,115E, \tag{1}$$

we calculated the $O - C$ values for those eclipse timings, which are plotted in the upper panel of Figure 2. The $O - C$ curve exhibits an upward parabolic trend, implying that IP Lyn is undergoing a secular increase in its orbital period. Using the `OCFit`[10] Python package (Gajdoš & Parimucha 2019), we adopted the quadratic polynomial to fit the $O - C$ curve and obtained a quadratic ephemeris

$$\begin{aligned}\mathrm{Min.I} &= \mathrm{HJD}2454501.47094(5)\\ &+ 0.489\,115\,60(2)E + 2.56(2) \times 10^{-10}E^2,\end{aligned} \tag{2}$$

which is depicted as a solid line in the upper panel of Figure 2. The corresponding residuals are displayed in the lower panel of Figure 2, where no significant trend can be found. By using the coefficient of the quadratic term, we determine the rate of secular period increase, $\dot{P} = 3.82(3) \times 10^{-7}$ day yr$^{-1}$.

[10] https://github.com/pavolgaj/OCFit

**Table 4**
Eclipse Timings of IP Lyn Collected from Literature and Calculated from Ground-based and Survey Observations

| JD(Hel.) | Error | Filter | Type | Reference |
|---|---|---|---|---|
| 2454432.99300[a] | 0.00148 | without filter | p | this paper |
| 2454433.24112[a] | 0.00136 | without filter | s | this paper |
| 2454497.55800[a] | 0.00060 | without filter | p | this paper |
| 2454501.47300 | … | 400–700 nm | p | Khruslov (2013) |
| 2454538.15596[a] | 0.00139 | 400–700 nm | p | this paper |
| 2454538.39650[a] | 0.00380 | 400–700 nm | s | this paper |
| 2456732.33199[b] | 0.00136 | *V* | p | this paper |
| 2456732.57882[b] | 0.00194 | *V* | s | this paper |
| 2457397.04239[b] | 0.00101 | *V* | p | this paper |
| 2457397.28660[b] | 0.00154 | *V* | s | this paper |
| 2458045.12431[b] | 0.00227 | *V* | p | this paper |
| 2458045.36739[b] | 0.00354 | *V* | s | this paper |
| 2458141.97399[c] | 0.00098 | *BVR* | p | this paper |
| 2458142.21724[c] | 0.00081 | *BVR* | s | this paper |
| 2458508.80574[d] | 0.00131 | *r* | p | this paper |
| 2458509.04813[d] | 0.00220 | *r* | s | this paper |
| 2458516.14496[d] | 0.00114 | *g* | p | this paper |
| 2458516.39501[d] | 0.00357 | *g* | s | this paper |
| 2458819.40277[d] | 0.00096 | *g* | p | this paper |
| 2458819.64997[d] | 0.00224 | *g* | s | this paper |
| 2458845.57586[e] | 0.00065 | 600–1000 nm | s | this paper |
| 2458845.82062[e] | 0.00119 | 600–1000 nm | p | this paper |
| 2458851.69064[e] | 0.00076 | 600–1000 nm | p | this paper |
| 2458851.93442[e] | 0.00029 | 600–1000 nm | s | this paper |
| 2458859.51542[e] | 0.00089 | 600–1000 nm | p | this paper |
| 2458859.76094[e] | 0.00028 | 600–1000 nm | s | this paper |
| 2458865.38475[e] | 0.00023 | 600–1000 nm | p | this paper |
| 2458865.63016[e] | 0.00038 | 600–1000 nm | s | this paper |
| 2458910.37823[d] | 0.00164 | *r* | p | this paper |
| 2458910.62934[d] | 0.00193 | *r* | s | this paper |
| 2459174.01323[d] | 0.00112 | *r* | p | this paper |
| 2459174.25914[d] | 0.00218 | *r* | s | this paper |
| 2459245.42350[d] | 0.00084 | *g* | p | this paper |
| 2459245.67049[d] | 0.00096 | *g* | s | this paper |
| 2459566.28648[d] | 0.00309 | *r* | p | this paper |
| 2459566.53233[d] | 0.00137 | *r* | s | this paper |
| 2459680.74212[d] | 0.00191 | *g* | p | this paper |
| 2459680.98863[d] | 0.00236 | *g* | s | this paper |

**Notes.**
[a] These times were derived from the photometric data of SuperWASP.
[b] These times were derived from the photometric data of ASAS-SN.
[c] These times were derived from our observations.
[d] These times were derived from the photometric data of ZTF.
[e] These times were derived from the photometric data of TESS.

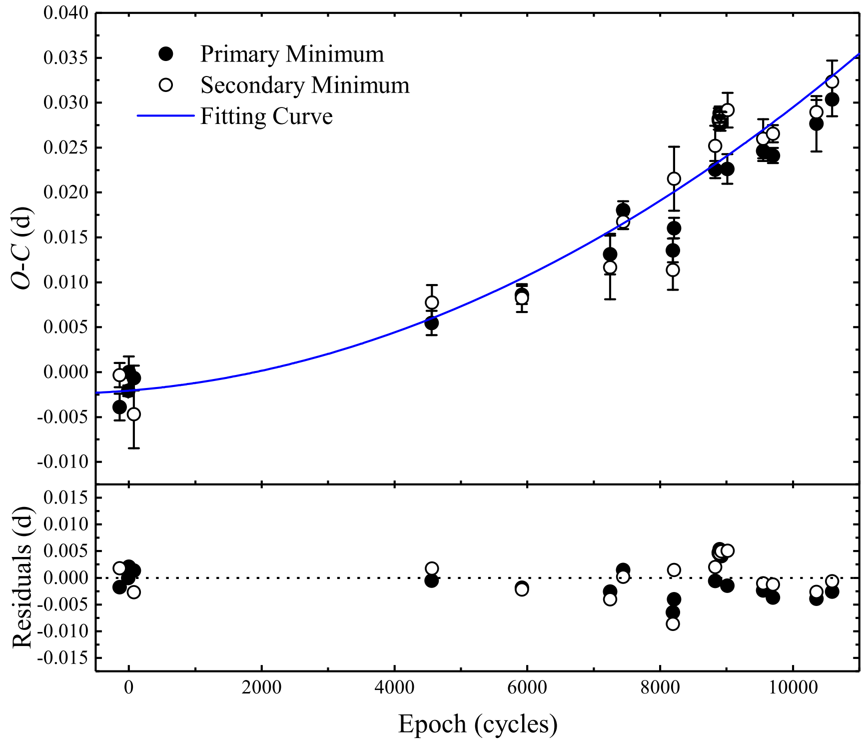


**Figure 2.** $O - C$ diagram for IP Lyn. The open and filled circles refer to the primary minimum and secondary minimum, respectively. The solid line is a fitting curve of the quadratic function. The corresponding residuals are plotted in the bottom panel. The dotted line represents the linear fit for the residuals.

## 4. Photometric Solutions and Absolute Parameters

The *BVR*-band photometric light curves of IP Lyn were simultaneously analyzed by using the `PHysics Of Eclipsing BinariEs` (`PHOEBE`) 2.4 (Prša & Zwitter 2005; Conroy et al. 2020; Jones et al. 2020). According to the LAMOST spectra, we adopted the primary's temperature of $T_1 = 6675$ K. Due to the convective envelope, we assumed the bolometric albedo coefficients $A_1 = A_2 = 0.5$ (Ruciński 1969) and gravity darkening coefficients $g_1 = g_2 = 0.32$ (Lucy 1967). The logarithmic limb-darkening law was applied and the corresponding coefficients were derived by the atmospheric model of Castelli & Kurucz (2004). In order to determine the preliminary mass ratio $q$ and orbital inclination $i$, we performed a two-dimensional grid search in the $q - i$ plane by employing the `PHOEBE` solver. During the $q - i$ scan, the primary's temperature $T_1$, the mass ratio $q$ and the orbital inclination $i$ were set as fixed parameters, while the secondary's temperature $T_2$, the dimensionless potential for two components $\Omega_1 = \Omega_2$ and the passband luminosity of the primary $L_1$ were set as adjustable parameters. In addition, from the light curve morphology, we could qualitatively conclude that IP Lyn is an A-subtype and a totally eclipsing contact binary with a relatively low mass ratio. Thus, it is reasonable to perform the search within the ranges of $q \in [0.02, 0.40]$ and $i \in [68, 90]$. The steps of $q$ and $i$ were set to be 0.01 and 1°, respectively. Figure 3 represents a two-dimensional distribution of the logarithmic value of chi-square $\log \chi^2$ in the $q - i$ plane, where a minimum value of $\log \chi^2$ is located at (0.06, 77°) (see the white cross in Figure 3).

Following the initial parameters and the results of the above test, we determine the most probabilistic parameters and the corresponding uncertainties by using the Markov Chain Monte Carlo (MCMC) method in `PHOEBE` via the `emcee` Python package (Foreman-Mackey et al. 2013). The final converging solution and the uncertainties of adjustable parameters are summarized in the second column of Table 5. In estimating the uncertainties of the adjustable parameters, we also consider the error of the LAMOST temperature. The theoretical light curves are plotted in Figure 4(a). Due to the slight asymmetry in the observed light curves, the solution cannot well reproduce the photometric data. Usually, the asymmetry of light curves can be interpreted as a result of spots on the surface of component stars. Because asymmetry in the light curve of IP Lyn can be observed at the 0.5 phase (the secondary star is fully eclipsed), the spot can be located only on the primary component. Thus, two alternative spot models: (1) a hot spot on the primary in the phase range of 0.25–0.50 and (2) a cool spot on the primary in the phase range of 0.5–0.75 can explain the light curve asymmetry of IP Lyn. By rerunning the MCMC parameter search, we obtained two photometric solutions corresponding

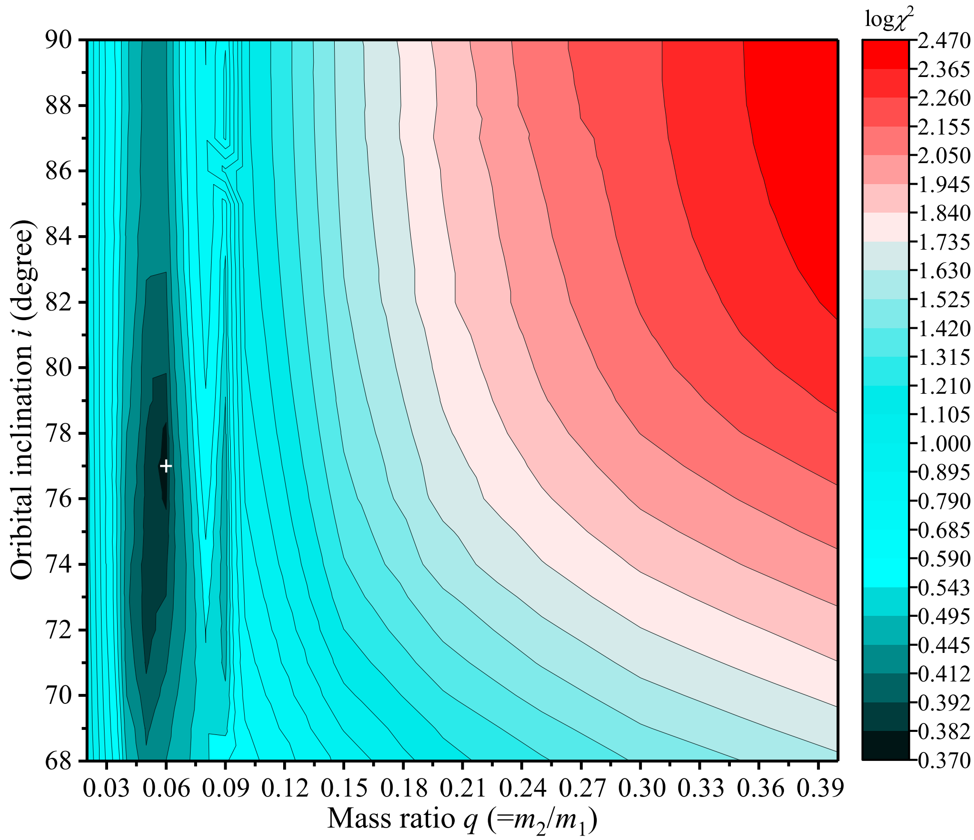


**Figure 3.** Contour plot of $\log\chi^2$ (color-coded according to the scale on the right) in the ($q$, $i$) plane for IP Lyn. The white cross represents the solution with the lowest value of $\log\chi^2$.

to the two spot models, which are summarized in the third and fourth columns of Table 5. The theoretical light curves are depicted in Figure 4(b) and (c). The parameter distributions determined by the MCMC sampling are shown in Figures 5 and 6. According to the values of $\chi^2$ for the two solutions with a spot, the cool spot model can better fit the observed light curves of IP Lyn than the hot spot model, implying the light curve asymmetry can be more plausibly caused by a cool spot on the primary star.

As has been mentioned, several survey projects have also observed our target and provided rich photometric data. According to the quantity and quality of these observations, we adopted the photometric data from three surveys: SuperWASP, TESS and ZTF, to perform the light curve investigations and check the above photometric solutions. Because the photometric data from SuperWASP exhibit a very large scatter, we excluded the data points with errors larger than $0^{\rm m}_{.}03$. For the photometric data from TESS and ZTF, we eliminated data points with a nonzero flag for the QUALITY parameter. During the analysis, the photometric solution with a cool spot determined by our observations was adopted as initial parameters. In addition, because IP Lyn was observed by TESS at a long cadence (30 minute cadence), we considered the phase-smearing effect during the analysis of TESS's light curve (Li et al. 2021b). The parameters and their uncertainties were also estimated with the same MCMC method. All photometric solutions for those surveys' observations are summarized in Table 5, and the synthetic light curves are depicted in Figure 4(d–f). Finally, as should be noted, the light curves from those surveys, especially the TESS light curve, did not exhibit any significant asymmetry. Thus, we did not consider the spot model to fit them. Of course, it also implies that the stellar spot detected from our multiple-band observations should be active. Perhaps, the stellar spot occurs just during our observations and disappears for the TESS observational period.

Owing to the absence of radial-velocity curves, we calculated the absolute parameters of IP Lyn by using two different methods. One is the Gaia-distance-based scheme proposed by Kjurkchieva et al. (2019a), developed by Liu et al. (2020), and Li et al. (2021b) demonstrated that the Gaia distance can be applied to estimate the absolute parameters for most contact binaries. The other is based on empirical relations to estimate the absolute parameters. Here we adopted the updated empirical relation between the semimajor axis and

**Table 5**
Photometric Solutions for Our *BVR*-band and Survey Light Curves

| Parameter | NAOC-85 cm | | | SuperWASP | TESS | ZTF |
|---|---|---|---|---|---|---|
| | Without Spot | Hot Spot | Cool Spot | Without Spot | Without Spot | Without Spot |
| $i$(deg) | $76.17^{+0.33}_{-0.70}$ | $77.07^{+0.41}_{-0.33}$ | $75.54^{+0.38}_{-0.26}$ | $74.96^{+0.70}_{-0.58}$ | $78.25^{+0.24}_{-0.16}$ | $76.82^{+0.44}_{-0.38}$ |
| $q = M_2/M_1$ | $0.0565^{+0.0017}_{-0.0006}$ | $0.0579^{+0.0002}_{-0.0001}$ | $0.0554^{+0.0005}_{-0.0001}$ | $0.0477^{+0.0005}_{-0.0008}$ | $0.0652^{+0.0001}_{-0.0012}$ | $0.0579^{+0.0011}_{-0.0003}$ |
| $T_1$ (K) | $6683^{+3}_{-7}$ | $6666^{+2}_{-2}$ | $6677^{+2}_{-3}$ | $6673^{+11}_{-11}$ | $6669^{+2}_{-2}$ | $6676^{+14}_{-12}$ |
| $T_2$ (K) | $6276^{+8}_{-16}$ | $6123^{+9}_{-12}$ | $6410^{+13}_{-10}$ | $6352^{+26}_{-24}$ | $6144^{+11}_{-5}$ | $6184^{+16}_{-17}$ |
| $\Omega_1 = \Omega_2$ | $1.8059^{+0.0070}_{-0.0031}$ | $1.8104^{+0.0007}_{-0.0010}$ | $1.8015^{+0.0016}_{-0.0005}$ | $1.7750^{+0.0018}_{-0.0032}$ | $1.8383^{+0.0006}_{-0.0005}$ | $1.8103^{+0.0044}_{-0.0017}$ |
| $\frac{L_1}{L_1+L_2}$ ($B$) | $0.9468^{+0.0015}_{-0.0039}$ | $0.9526^{+0.0014}_{-0.0009}$ | $0.9405^{+0.0016}_{-0.0011}$ | … | … | … |
| $\frac{L_1}{L_1+L_2}$ ($V$) | $0.9420^{+0.0012}_{-0.0032}$ | $0.9465^{+0.0011}_{-0.0011}$ | $0.9373^{+0.0013}_{-0.0009}$ | … | … | … |
| $\frac{L_1}{L_1+L_2}$ ($R$) | $0.9390^{+0.0015}_{-0.0032}$ | $0.9425^{+0.0010}_{-0.0009}$ | $0.9352^{+0.0014}_{-0.0009}$ | … | … | … |
| $\frac{L_1}{L_1+L_2}$ (WASP) | … | … | … | $0.9464^{+0.0027}_{-0.0024}$ | … | … |
| $\frac{L_1}{L_1+L_2}$ (TESS) | … | … | … | … | $0.9349^{+0.0006}_{-0.0004}$ | … |
| $\frac{L_1}{L_1+L_2}$ (ZTFg) | … | … | … | … | … | $0.9474^{+0.0015}_{-0.0012}$ |
| $\frac{L_1}{L_1+L_2}$ (ZTFr) | … | … | … | … | … | $0.9415^{+0.0014}_{-0.0013}$ |
| $r_1$ | $0.6264^{+0.0010}_{-0.0025}$ | $0.6249^{+0.0004}_{-0.0003}$ | $0.6278^{+0.0002}_{-0.0005}$ | $0.6366^{+0.0011}_{-0.0006}$ | $0.6155^{+0.0017}_{-0.0002}$ | $0.6249^{+0.0007}_{-0.0015}$ |
| $r_2$ | $0.1790^{+0.0012}_{-0.0004}$ | $0.1800^{+0.0002}_{-0.0003}$ | $0.1778^{+0.0005}_{-0.0002}$ | $0.1686^{+0.0007}_{-0.0008}$ | $0.1852^{+0.0002}_{-0.0002}$ | $0.1805^{+0.0007}_{-0.0004}$ |
| $\theta$ (deg) (fixed) | … | 90 | 90 | … | … | … |
| $\lambda$ (deg) | … | $302.4^{+2.5}_{-2.1}$ | $47.4^{+2}_{-3.4}$ | … | … | … |
| $r_s$ (deg) | … | $10.7^{+0.8}_{-0.5}$ | $13.0^{+0.4}_{-0.4}$ | … | … | … |
| $T_s/T_1$ | … | $1.055^{+0.006}_{-0.007}$ | $0.939^{+0.002}_{-0.002}$ | … | … | … |
| $f = \frac{\Omega_{in} - \Omega}{\Omega_{in} - \Omega_{out}}$ | $21.8^{+1.4}_{-2.5}\%$ | $21.1^{+0.9}_{-0.8}\%$ | $21.4^{+0.3}_{-0.2}\%$ | $16.9^{+1.9}_{-1.7}\%$ | $15.4^{+2}_{-0.6}\%$ | $22.0^{+2.1}_{-1.9}\%$ |
| $\frac{\sum_i (O_i - C_i)^2}{N}$ | $1.193 \times 10^{-4}$ | $1.049 \times 10^{-4}$ | $0.945 \times 10^{-4}$ | $5.730 \times 10^{-4}$ | $0.113 \times 10^{-4}$ | $1.375 \times 10^{-4}$ |
| $\chi^2$ | 2.280 | 1.991 | 1.768 | 1.938 | … | 1.186 |

orbital period derived by Yu et al. (2022). By a combination of the photometric solution with the cool spot model and the two methods, the absolute parameters of IP Lyn were determined and are listed in Table 6. As can be seen from Table 6, the absolute parameters estimated by the empirical relation are very consistent with those determined from the Gaia-distance-based scheme, implying that they should be reliable.

## 5. Discussions and Conclusion

The above orbital period investigation suggested that IP Lyn is undergoing a secular period increase. The secular period increase may, in general, be interpreted as a result of mass transfer from the less massive secondary to the more massive primary. By inserting the absolute physical parameters into the following equation (Pringle 1975)

$$\dot{M}_1 = -\dot{M}_2 = \frac{\dot{P}}{3P} \cdot \frac{M_1 M_2}{(M_1 - M_2)}. \quad (3)$$

we calculated a mass-transfer rate of $\dot{M}_1 = 2.66 \times 10^{-8}\ M_\odot\ \mathrm{yr}^{-1}$. Accordingly, the mass transfer timescale of the less massive secondary can be estimated as $\tau_{mt} = 3.63 \times 10^6$ yr. According to the definition of the Kelvin–Helmholtz thermal timescale ($\tau_{th} \sim \frac{GM^2}{RL}$, Paczyński 1971), we estimated the thermal timescale of the secondary as $\tau_{th} = 6.64 \times 10^5$ yr. Apparently, the thermal timescale is significantly shorter than the mass-transfer timescale, implying that the secondary star can maintain thermal equilibrium or stable mass transfer.

In principle, the continuous mass transfer from the secondary to the primary can yield an impact spot on the surface of the primary. Owing to the Coriolis force, the impact spot can, in general, be located on a longitude range from 0° to 90° and may be observed in the phase range from 0.75 to 1.0, just like V361 Lyr (Hilditch et al. 1997), CN And (Van Hamme et al. 2001) and GR Tau (Qian 2002). For IP Lyn, the contact configuration cannot provide any space between the primary's surface and the inner Lagrangian point to allow the impact spot to reach a relatively large longitude. At the same time, the accreting energy should be also negligible due to the contact configuration. Together with the relatively large temperature difference (about 500 K), we may infer that the impact spot should be cool with a very small longitude. However, the optimal photometric solution suggests that the location of the cool spot is not in agreement with that of the impact spot. Moreover, from the high-precision TESS light curve, we cannot find any significant asymmetries. This means that the asymmetry observed in our *BVR*-band light curves was not indeed permanent and stable. Thus, the spot suggested by the photometric solutions should be a magnetic one, rather than an impact one caused by the continuous mass transfer.

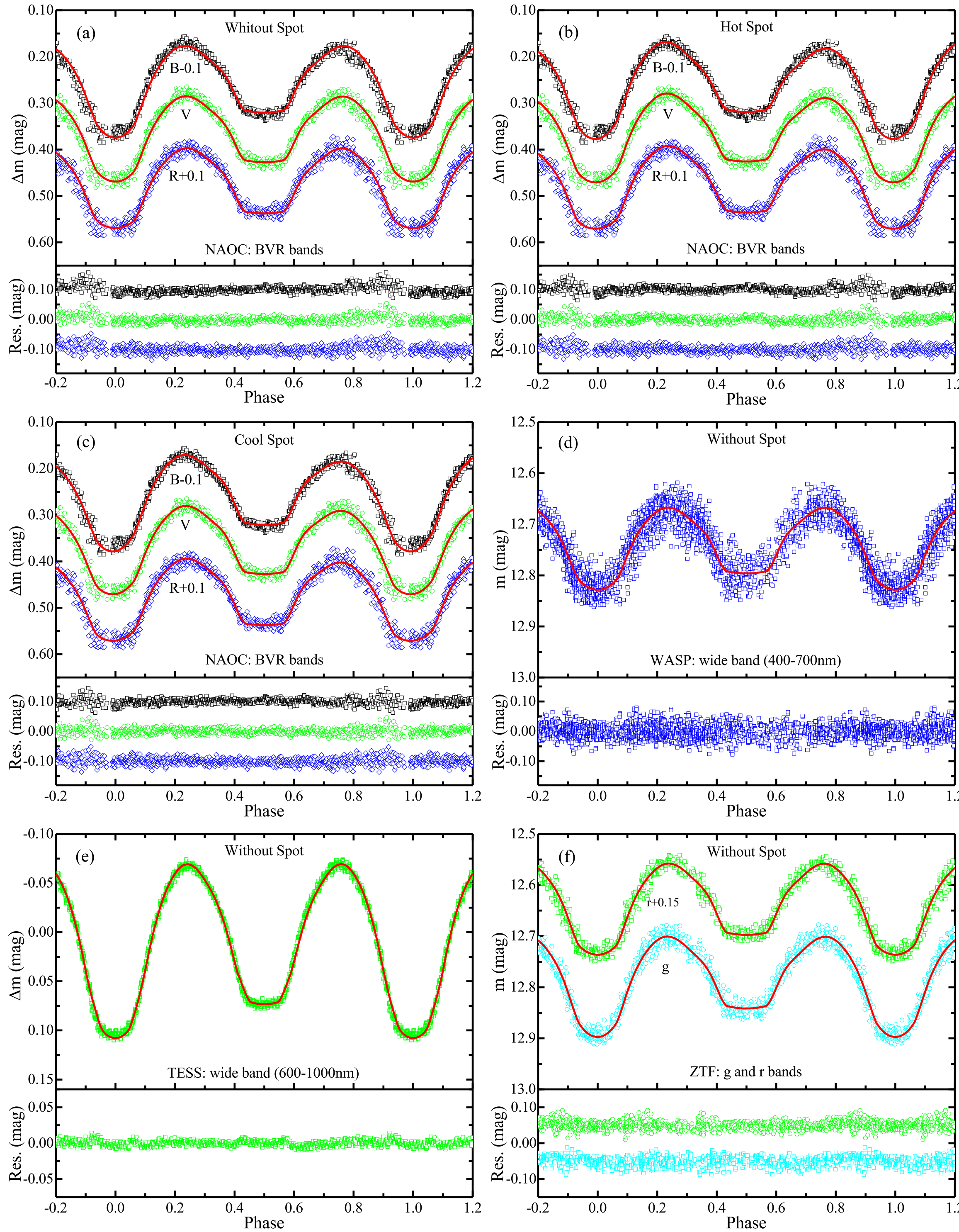


**Figure 4.** Observed (hollow symbols) and theoretical (solid lines) light curves for IP Lyn. The residuals are shown in the corresponding lower panels.

Of course, the secular orbital period could be also a part of the long-period oscillation caused by an underlying third body. If so, the system's velocity (i.e., the so-called gamma velocity $V_{\gamma}$) will gradually change with the movement of the binary system orbiting the center of mass for the three bodies. Three radial velocities derived from three LAMOST spectra somewhat deviate from each other, plausibly indicating a continuous change of $V_{\gamma}$. However, for an ELMRCB, these radial velocities

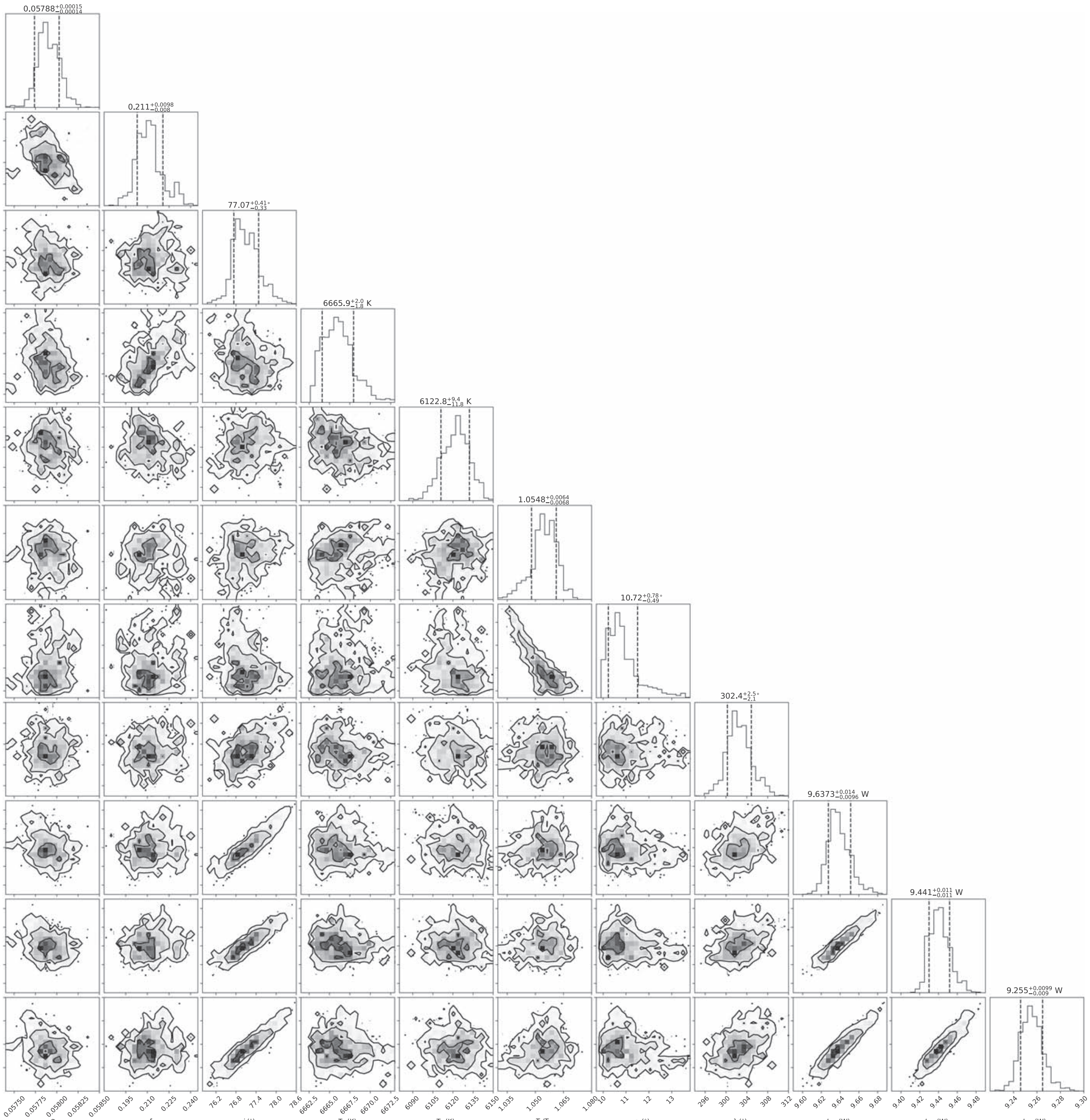

**Figure 5.** Probability distribution of the free adjustable parameters in the hot spot model for the *BVR* band light curves of IP Lyn.

determined from the LAMOST spectral observations should be associated with those of its primary component because the spectral lines of the secondary component are rather faint and even invisible. Additionally, the radial velocity of the primary component of an ELMRCB contributed by its orbital movement is very small. Moreover, the median phases of three LAMOST spectral observations are very close to 0.0 or 0.5. Therefore, the three velocities of IP Lyn derived from the LAMOST spectra could be practically the system's velocity. However, it should be noted that the epochs corresponding to three observation median Heliocentric Julian Dates (HJDs) are just around the minimum of the $O-C$ curve (i.e., the trough of the $O-C$ curve if it is

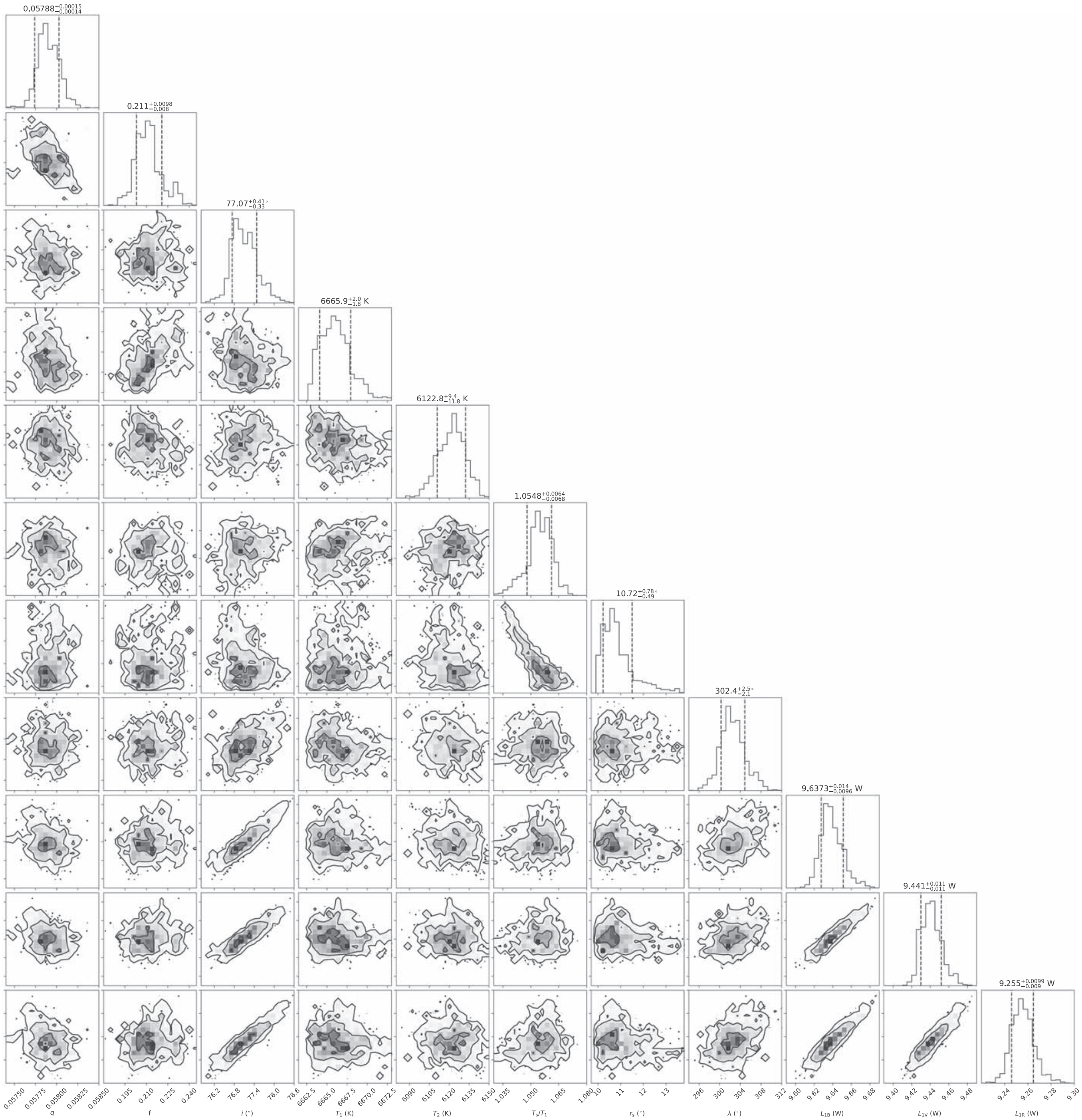

**Figure 6.** Probability distribution of the free adjustable parameters in the cool spot model for the *BVR* band light curves of IP Lyn.

indeed a part of the periodic oscillation). In this case, $V_\gamma$ should be continuously increasing. But the observed radial velocities gradually decreased from $-41.00$ to $-52.87$ km s$^{-1}$. This contradiction indicates the absence of a third body. Of course, it is also possibly caused by the uncertainty of measurements due to the low-resolution spectral observations.

In order to analyze the evolutionary status of IP Lyn, we located its two components in the $\log M/M_\odot - \log L/L_\odot$ and $\log M/M_\odot - \log R/R_\odot$ diagrams (Figure 7). For comparison, we performed a careful search for contact binaries from the literature and selected 117 samples with mass ratio lower than 0.15 (see Table 7). We classified them as ELMRCBs and added

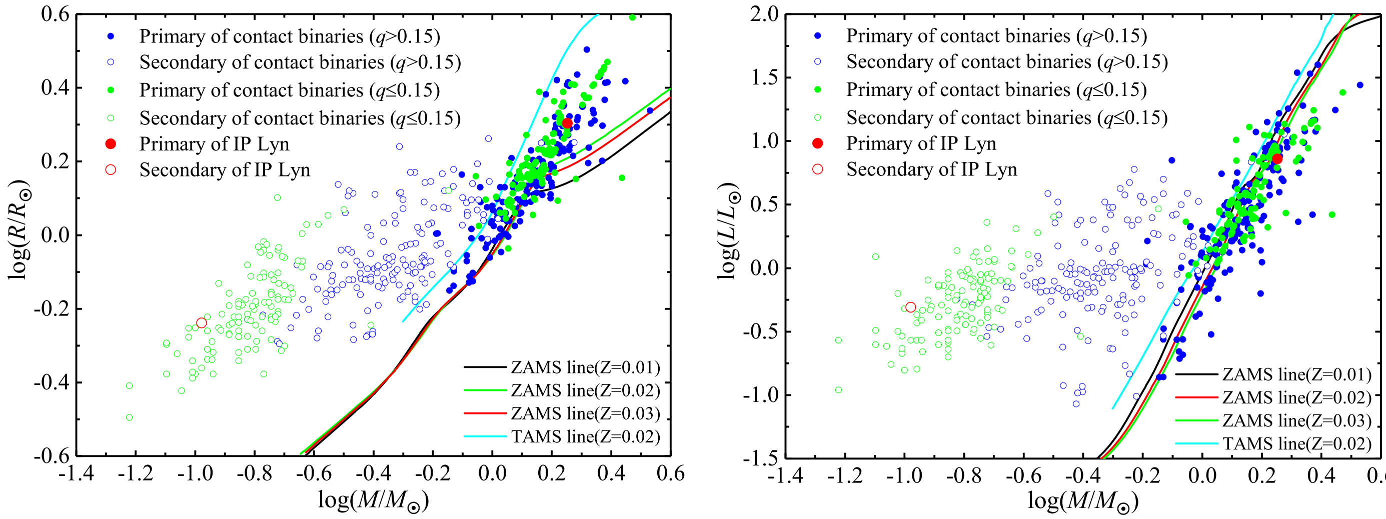


**Figure 7.** Mass–radius (left panel) and mass–luminosity (right panel) relation diagrams.

**Table 6**
Absolute Physical Parameters for IP Lyn Estimated by Two Different Methods

| Method | $A$ ($R_\odot$) | $M_1$ ($M_\odot$) | $M_2$ ($M_\odot$) | $R_1$ ($R_\odot$) | $R_2$ ($R_\odot$) | $L_1$ ($L_\odot$) | $L_2$ ($L_\odot$) |
|---|---|---|---|---|---|---|---|
| GD | $3.203^{+0.235}_{-0.236}$ | $1.744^{+0.384}_{-0.386}$ | $0.097^{+0.022}_{-0.022}$ | $2.011^{+0.148}_{-0.150}$ | $0.569^{+0.043}_{-0.043}$ | $7.247^{+1.074}_{-1.091}$ | $0.494^{+0.079}_{-0.077}$ |
| ER | $3.297^{+0.096}_{-0.096}$ | $1.903^{+0.166}_{-0.166}$ | $0.105^{+0.010}_{-0.009}$ | $2.070^{+0.060}_{-0.062}$ | $0.586^{+0.018}_{-0.018}$ | $7.681^{+0.458}_{-0.471}$ | $0.523^{+0.037}_{-0.035}$ |

**Note.** GD and ER denote the Gaia-distance-based method and the empirical relation, respectively. The errors are calculated according to the error propagation rule.

them to these diagrams. In Figure 7, the Zero-Age Main Sequence (ZAMS) and Terminal-Age Main Sequence (TAMS) lines are calculated by using the PARSEC models[11] (Bressan et al. 2012). Similar to other ELMRCBs, the primary component of IP Lyn is located on the main sequence belt, while the secondary component exhibits over-sized and over-luminous characteristics relative to a normal main sequence star with the same mass. In general, the over-size and over-luminosity phenomena for the less massive component of a contact binary may have resulted from energy transfer from the more massive primary to the less massive secondary (Lucy 1968; Moses 1976). However, it should be noted that the radii of the secondary components are about four times larger than a corresponding main sequence star with the same mass. Obviously, it is physically hard to inflate a main sequence star to such large size purely by the energy transfer from its more massive companion (Stępień 2004). So, the less massive secondary should be more evolved with hydrogen depleted in its center. In addition, we calculated the orbital angular momentum for these systems with the following formula

$$J_{\rm orb} = A^2 \frac{M_1 M_2}{M_1 + M_2} \cdot \frac{2\pi}{P}, \quad (4)$$

and located them on the diagram of $\log J_{\rm orb}$ versus $\log M_{\rm tot}$ ($M_{\rm tot} = M_1 + M_2$ denotes the total mass). In Figure 8, we also added 119 detached binaries collected by Eker et al. (2006) and 159 contact binaries with a mass ratio larger than 0.15. These contact binaries were selected from the recent catalog compiled by Yu et al. (2022). Clearly, the location of IP Lyn is under the borderline derived by Eker et al. (2006), which confirms the contact geometrical configuration of IP Lyn. In addition, it should be noted that the orbital angular momenta of ELMRCBs are, in general, significantly lower than those of contact binaries with relatively high mass ratios. Due to the angular momentum loss during the evolution of a contact binary, the significantly low orbital angular momenta seem to indicate that ELMRCBs are at the late evolutionary stage of a contact binary.

The photometric solutions for both our ground-based and several surveys' observations suggested that IP Lyn is an ELMRCB. Moreover, its mass ratio ($q \sim 0.055$) is lower than the theoretical limit ($q_{\rm min} = 0.071 \sim 0.078$) predicted by the traditional models (Rasio 1995; Li & Zhang 2006), and also close to the lower limit of the mass ratio ($q_{\rm min} = 0.05$) determined by taking the primary's mass and structure into account (Jiang et al. 2010). In order to examine the dynamical stability of IP Lyn, we employed the following equation

[11] http://stev.oapd.inaf.it/cgi-bin/cmd

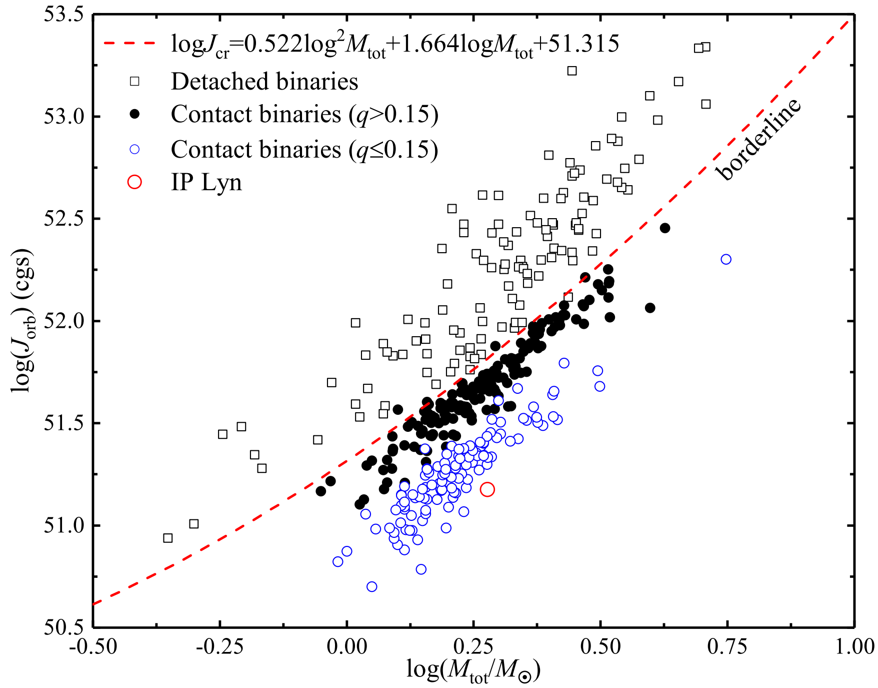


**Figure 8.** Location of IP Lyn (red open circle) in the $\log J_{orb} - \log M_{tot}$ diagram. The detached binaries (open squares) are taken from the catalog of chromospherically active binaries compiled by Eker et al. (2006). The contact binaries with mass ratios larger than 0.15 (solid circles) are selected from the catalog compiled by Yu et al. (2022). The ELMRCBs (open circles) are taken from Table 7. The red dashed line represents the boundary between detached and contact binaries derived by Eker et al. (2006).

**Table 7**
Physical Parameters of 117 Extremely Low Mass Ratio Contact Binaries

| Name | Period | $A(R_\odot)$ | $T_1$(K) | $T_2$(K) | $M_1(M_\odot)$ | $M_2(M_\odot)$ | $R_1(R_\odot)$ | $R_2(R_\odot)$ | $L_1(L_\odot)$ | $L_2(L_\odot)$ | $q$ | Reference |
|---|---|---|---|---|---|---|---|---|---|---|---|---|
| V1187 Her | 0.31076 | 2.161 | 6250 | 6651 | 1.340 | 0.060 | 1.410 | 0.390 | 2.750 | 0.270 | 0.044 | 1 |
| VSX J082700.8+462850 | 0.27716 | 1.858 | 5870 | 5828 | 1.060 | 0.060 | 1.150 | 0.320 | 1.400 | 0.110 | 0.055 | 2 |
| KIC 4244929 | 0.34140 | 2.388 | 5857 | 5867 | 1.481 | 0.087 | 1.521 | 0.477 | 2.440 | 0.242 | 0.059 | 3 |
| KIC 9151972 | 0.38680 | 2.666 | 6040 | 5982 | 1.606 | 0.095 | 1.696 | 0.528 | 3.431 | 0.318 | 0.059 | 3 |
| KIC 11097678 | 0.99972 | 6.165 | 6493 | 6334 | 2.960 | 0.189 | 3.897 | 1.264 | 24.180 | 2.290 | 0.064 | 3 |
| ... | ... | ... | ... | ... | ... | ... | ... | ... | ... | ... | ... | ... |
| CSS_J022044.4+280006 | 0.75938 | 4.536 | 6760 | 6382 | 1.890 | 0.280 | 2.560 | 1.130 | 13.640 | 1.900 | 0.150 | 7 |
| TYC 4157−0683−1 | 0.39607 | 2.640 | 6037 | 5888 | 1.367 | 0.206 | 1.499 | 0.667 | 2.692 | 0.482 | 0.150 | 51 |
| CSS_J080724.7+164610 | 0.36296 | 2.419 | 5984 | 6022 | 1.250 | 0.190 | 1.370 | 0.610 | 1.860 | 0.440 | 0.150 | 7 |
| CSS_J051156.6+011756 | 0.75272 | 4.381 | 6414 | 5936 | 1.730 | 0.260 | 2.450 | 1.070 | 8.760 | 1.280 | 0.150 | 7 |
| CSS_J163819.6+034852 | 0.20533 | 1.599 | 6665 | 6649 | 1.130 | 0.170 | 0.920 | 0.420 | 1.130 | 0.310 | 0.150 | 7 |

**Note.** The full data set of Table 7 is compiled as a supplementary file (mst2-mrt.txt) in machine-readable format. Here a portion is presented for guidance regarding its form and content.

**References.** 1. Caton et al. 2019; 2. Li et al. 2021a; 3. Śenavcı et al. 2016; 4. Qian et al. 2005; 5. Gazeas et al. 2021a; 6. Sriram et al. 2016; 7. Christopoulou et al. 2022; 8. Kjurkchieva et al. 2018a; 9. Elkhateeb & Nouh 2014; 10. Li et al. 2017; 11. Wadhwa et al. 2021a; 12. Zola et al. 2004; 13. Liu et al. 2023; 14. Wadhwa 2006; 15. Szalai et al. (2007); 16. Gazeas et al. (2021b); 17. Li et al. (2022); 18. Gazeas et al. (2006); 19. Deb & Singh (2011); 20. El-Sadek et al. (2019); 21. Broens (2013); 22. Pribulla & Rucinski (2008); 23. Rucinski (2015); 24. Yang (2008); 25. Śenavcı et al. (2008); 26. Alton (2018); 27. Kandulapati et al. (2015); 28. Ekmekći et al. (2012); 29. Saygan (2016); 30. Wadhwa et al. (2021b); 31. Kjurkchieva et al. (2018b); 32. Yang et al. (2012); 33. Zola et al. (2010); 34. Liu et al. (2015); 35. Kjurkchieva et al. (2019b);36. Tian et al. (2019); 37.Wadhwa (2005); 38. Gazeas et al. (2005); 39.Liu et al. (2011); 40. Yang et al. (2005); 41.Zhou et al. (2016); 42. Gezer & Bozkurt (2016); 43. Yang et al. (2013); 44. Liu et al. (2014); 45. Luo et al. (2017); 46. Michel & Kjurkchieva (2019); 47. Oh et al. (2007); 48. Li et al. (2020); 49. Bulut et al. (2016); 50. Qian et al. (2008); 51. Acerbi et al. (2014).

derived by Yang & Qian (2015)

$$\frac{J_{spin}}{J_{orb}} = \frac{1+q}{q}[(k_1 r_1)^2 + (k_2 r_2)^2 q], \tag{5}$$

to calculate the ratio of spin to orbital angular momentum. In this equation, the gyration radius $k_1$ of the primary star was estimated according to the empirical relation $k_1 = 0.014M + 0.152$ derived by Landin et al. (2009). Because of the very low mass of the secondary component of IP Lyn, we can assume that the secondary is a fully convective star and thus set $k_2^2 = 0.205$ (Arbutina 2007). Finally, we obtained the ratio of spin to orbital angular momentum of IP Lyn as $J_{\rm spin}/J_{\rm orb} = 0.240$. It is significantly smaller than 1/3, suggesting that the system is currently stable. Recently, Wadhwa et al. (2021a, 2021) derived the instability mass ratio, the instability separation and the instability orbital period. These instability parameters are dependent on the primary's mass and the contact degree of the binary system and provide a criterion to assess orbital instability of a contact binary. By inserting the absolute parameters into Equations (10) and (13) of Wadhwa et al. (2021a), and Equation (8) of Wadhwa et al. (2021), we calculated the instability mass ratio, separation and period for IP Lyn as $q_{\rm inst} = 0.045$, $A_{\rm inst} = 2.908\ R_\odot$ and $P_{\rm inst} = 0.423$ d respectively. The gyration radius for the primary and secondary stars was the same as the above calculations. Clearly, the current mass ratio ($q = 0.055$), separation ($A = 3.203\ R_\odot$) and period ($P = 0.489$ d) are all significantly higher than the corresponding instability parameters, implying that IP Lyn should be currently stable.

In summary, we have performed the first photometric and orbital period investigations for the totally eclipsing binary IP Lyn. The solutions for several sets of light curves from both the ground-based and surveys' observations suggested that it is an ELMRCB ($q \sim 0.055$) with a relatively shallow contact degree ($f \sim 21.4\%$). The extremely low mass ratio indicates that it might be an underlying progenitor of a luminous red nova. However, because the current physical parameters are significantly lower than the corresponding instability parameters, the system can be still stable currently. Based on the analysis of the eclipse timings, we ascertained that IP Lyn is undergoing a secular orbital period increase, which is likely caused by the continuous mass transfer from its less massive secondary to the more massive primary. As a result, the mass ratio of IP Lyn would further decrease to approach or reach the theoretical limit (Hut 1980; Rasio 1995; Jiang et al. 2010; Yang & Qian 2015). Based on the gradually decreasing mass ratio and the relatively low orbital angular momentum, it should be considered as a potential merger candidate. Thus, it is necessary to perform follow-up photometric and spectroscopic observations to determine the behavior of orbital period variation and track its subsequent evolution.

## Acknowledgments

This work is supported by the Joint Research Funds in Astronomy under a cooperative agreement between the National Natural Science Foundation of China (NSFC) and the Chinese Academy of Sciences (Nos. U1931115 and U2031114), and Scientific Research Fund of Hunan Provincial Education Department grant No. 22A0099. We acknowledge the support of the staff of the Xinglong 85 cm telescope. This work was partially supported by the Open Project Program of the Key Laboratory of Optical Astronomy, National Astronomical Observatories, Chinese Academy of Sciences.

We acknowledge the following surveys for their valuable spectroscopic or photometric data: (1) Guoshoujing Telescope (the Large Sky Area Multi-Object Fiber Spectroscopic Telescope, LAMOST) which is a National Major Scientific Project built by the Chinese Academy of Sciences. Funding for the project has been provided by the National Development and Reform Commission. LAMOST is operated and managed by the National Astronomical Observatories, Chinese Academy of Sciences; (2) the European Space Agency (ESA) mission Gaia[12] (Gaia Collaboration et al. 2016, 2018), processed by the Gaia Data Processing and Analysis Consortium (DPAC[13]). Funding for the DPAC has been provided by national institutions, in particular the institutions participating in the Gaia Multilateral Agreement; (3) the Wide Angle Search for Planets (WASP), where the data we used are from the DR1 of the WASP data (Butters et al. 2010) as provided by the WASP consortium, and the computing and storage facilities at the CERIT Scientific Cloud, reg. No. CZ.1.05/3.2.00/08.0144 which is operated by Masaryk University, Czech Republic; (4) The All-Sky Automated Survey for Supernovae (ASAS-SN, Shappee et al. 2014; Jayasinghe et al. 2018), which consists of two telescopes on a common mount which is hosted by Las Cumbres Observatory Global Telescope Network in the Faulkes Telescope North enclosure on Mount Haleakala, Hawaii; (5) ZTF (Bellm et al. 2019), which is a fully automated, wide-field survey aimed at a systematic exploration of the optical transient sky; and (6) the Transiting Exoplanet Survey Satellite (TESS, Ricker et al. 2015) mission. Funding for the TESS mission is provided by NASA's Science Mission Directorate.

## Appendix
## Supplementary Materials

The full data for Tables 2 and 7 are presented as the supplementary files: mst1-mrt.txt and mst2-mrt.txt, respectively.

## References

Acerbi, F., Barani, C., & Martignoni, M. 2014, NewA, 31, 1
Alton, K. B. 2018, JAAVSO, 46, 3
Arbutina, B. 2007, MNRAS, 377, 1635
Arbutina, B. 2012, POBeo, 91, 391
Bellm, E. C., Kulkarni, S. R., Graham, M. J., et al. 2019, PASP, 131, 018002
Borkovits, T., Rappaport, S., Hajdu, T., & Sztakovics, J. 2015, MNRAS, 448, 946
Bressan, A., Marigo, P., Girardi, L., et al. 2012, MNRAS, 427, 127
Broens, E. 2013, MNRAS, 430, 3070
Bulut, A., Bulut, İ., & Demircan, O. 2016, NewA, 44, 35
Butters, O. W., West, R. G., Anderson, D. R., et al. 2010, A&A, 520, L10
Castelli, F., & Kurucz, R. L. 2004, A&A, 419, 725

[12] https://www.cosmos.esa.int/gaia
[13] https://www.cosmos.esa.int/web/gaia/dpac/consortium

Caton, D., Gentry, D. R., Samec, R. G., et al. 2019, PASP, 131, 054203
Christopoulou, P.-E., Lalounta, E., Papageorgiou, A., et al. 2022, MNRAS, 512, 1244
Conroy, K. E., Kochoska, A., Hey, D., et al. 2020, ApJS, 250, 34
Counselman, C. C. I. 1973, ApJ, 180, 307
Darwin, G. H. 1908, RSPSA, 80, 166
Davenport, J. R. A., Becker, A. C., West, A. A., et al. 2013, ApJ, 764, 62
Deb, S., & Singh, H. P. 2011, MNRAS, 412, 1787
Eggleton, P. P. 2012, JASS, 29, 145
Eker, Z., Demircan, O., Bilir, S., & Karataş, Y. 2006, MNRAS, 373, 1483
Ekmekçi, F., Elmaslı, A., Yılmaz, M., et al. 2012, NewA, 17, 603
Elkhateeb, M. M., & Nouh, M. I. 2014, Ap&SS, 352, 673
El-Sadek, M. A., Djurašević, G., Essam, A., et al. 2019, NewA, 69, 21
Foreman-Mackey, D., Hogg, D. W., Lang, D., & Goodman, J. 2013, PASP, 125, 306
Gaia Collaboration, Brown, A. G. A., Vallenari, A., et al. 2018, A&A, 616, A1
Gaia Collaboration, Eyer, L., Rimoldini, L., et al. 2019, A&A, 623, A110
Gaia Collaboration, Prusti, T., de Bruijne, J. H. J., et al. 2016, A&A, 595, A1
Gaia Collaboration, Smart, R. L., Sarro, L. M., et al. 2020, A&A, 649, A6
Gajdoš, P., & Parimucha, Š 2019, OCFit: Python package for fitting of O-C diagrams, Astrophysics Source Code Library, ascl:1901.002
Gazeas, K., Zola, S., Liakos, A., et al. 2021b, MNRAS, 501, 2897
Gazeas, K. D., Baran, A., Niarchos, P., et al. 2005, AcA, 55, 123
Gazeas, K. D., Loukaidou, G. A., Niarchos, P. G., et al. 2021a, MNRAS, 502, 2879
Gazeas, K. D., Niarchos, P. G., Zola, S., Kreiner, J. M., & Rucinski, S. M. 2006, AcA, 56, 127
Gezer, İ., & Bozkurt, Z. 2016, NewA, 44, 40
Hilditch, R. W., Collier Cameron, A., Hill, G., Bell, S. A., & Harries, T. J. 1997, MNRAS, 291, 749
Hut, P. 1980, A&A, 92, 167
Jayasinghe, T., Kochanek, C. S., Stanek, K. Z., et al. 2018, MNRAS, 477, 3145
Jiang, D., Han, Z., Wang, J., Jiang, T., & Li, L. 2010, MNRAS, 405, 2485
Jones, D., Conroy, K. E., Horvat, M., et al. 2020, ApJS, 247, 63
Kandulapati, S., Devarapalli, S. P., & Pasagada, V. R. 2015, MNRAS, 446, 510
Khruslov, A. V. 2013, PZP, 13, 16
Kjurkchieva, D. P., Popov, V. A., Eneva, Y., & Petrov, N. I. 2019a, RAA, 19, 014
Kjurkchieva, D. P., Popov, V. A., & Petrov, N. I. 2018a, RAA, 18, 129
Kjurkchieva, D. P., Popov, V. A., & Petrov, N. I. 2018b, AJ, 156, 77
Kjurkchieva, D. P., Popov, V. A., & Petrov, N. I. 2019b, AJ, 158, 186
Kobulnicky, H. A., Molnar, L. A., Cook, E. M., & Henderson, L. E. 2022, ApJS, 262, 12
Kochanek, C. S., Shappee, B. J., Stanek, K. Z., et al. 2017, PASP, 129, 104502
Kwee, K. K., & van Woerden, H. 1956, BAIN, 12, 327
Landin, N. R., Mendes, L. T. S., & Vaz, L. P. R. 2009, A&A, 494, 209
Li, K., Gao, X., Liu, X.-Y., et al. 2022, AJ, 164, 202
Li, K., Hu, S., Chen, X., & Guo, D. 2017, PASJ, 69, 79
Li, K., Xia, Q.-Q., Kim, C.-H., et al. 2021a, ApJ, 922, 122
Li, K., Xia, Q.-Q., Kim, C.-H., et al. 2021b, AJ, 162, 13
Li, L., & Zhang, F. 2006, MNRAS, 369, 2001
Li, X.-Z., Liu, L., & Zhang, X.-D. 2020, PASJ, 72, 66
Liu, L., Chen, W. P., Na, W. W., et al. 2014, NewA, 31, 60
Liu, L., Qian, S., Li, K., et al. 2020, Ap&SS, 365, 71
Liu, L., Qian, S. B., & Fernández-Lajús, E. 2011, MNRAS, 415, 1509
Liu, L., Qian, S.-B., Soonthornthum, B., et al. 2015, PASJ, 67, 74
Liu, X.-Y., Li, K., Michel, R., et al. 2023, MNRAS, 519, 5760
Lucy, L. B. 1967, ZAp, 65, 89
Lucy, L. B. 1968, ApJ, 151, 1123
Luo, A. L., Zhao, Y.-H., Zhao, G., et al. 2015, RAA, 15, 1095
Luo, X., Wang, K., Zhang, X., et al. 2017, AJ, 154, 99
Mason, E., & Shore, S. N. 2022, A&A, 664, A12
Michel, R., & Kjurkchieva, D. 2019, NewA, 68, 51
Moses, A. P. 1976, MNRAS, 176, 161
Nefs, S. V., Birkby, J. L., Snellen, I. A. G., et al. 2012, MNRAS, 425, 950
Oh, K. D., Kim, C. H., Kim, H. I., & Lee, W. B. 2007, in ASP Conf. Ser. 362, The Seventh Pacific Rim Conf. Stellar Astrophysics, ed. Y. W. Kang et al. (San Francisco, CA: ASP), 82
Paczyński, B. 1971, ARA&A, 9, 183
Pešta, M., & Pejcha, O. 2023, A&A, 672, A176
Pribulla, T., & Rucinski, S. M. 2008, in Multiple Stars Across the H-R Diagram, ed. S. Hubrig, M. Petr-Gotzens, & A. Tokovinin (Berlin: Springer), 163
Pringle, J. E. 1975, MNRAS, 170, 633
Prša, A., & Zwitter, T. 2005, ApJ, 628, 426
Qian, S. 2002, MNRAS, 336, 1247
Qian, S., Yang, Y., Zhu, L., He, J., & Yuan, J. 2006, Ap&SS, 304, 25
Qian, S. B., He, J. J., Soonthornthum, B., et al. 2008, AJ, 136, 1940
Qian, S. B., Zhu, L. Y., Soonthornthum, B., et al. 2005, AJ, 130, 1206
Rasio, F. A. 1995, ApJL, 444, L41
Rasio, F. A., & Shapiro, S. L. 1995, ApJ, 438, 887
Ricker, G. R., Winn, J. N., Vanderspek, R., et al. 2015, JATIS, 1, 014003
Ruciński, S. M. 1967, AcA, 17, 271
Ruciński, S. M. 1969, AcA, 19, 245
Rucinski, S. M. 1992, AJ, 103, 960
Rucinski, S. M. 2007, MNRAS, 382, 393
Rucinski, S. M. 2015, AJ, 149, 49
Rucinski, S. M., Lu, W., Mochnacki, S. W., Ogłoza, W., & Stachowski, G. 2001, AJ, 122, 1974
Saygan, S. 2016, NewA, 46, 94
Şenavcı, H. V., Doğruel, M. B., Nelson, R. H., Yılmaz, M., & Selam, S. O. 2016, PASA, 33, e043
Şenavcı, H. V., Nelson, R. H., Özavcı, İ., Selam, S. O., & Albayrak, B. 2008, NewA, 13, 468
Shappee, B. J., Prieto, J. L., Grupe, D., et al. 2014, ApJ, 788, 48
Sriram, K., Malu, S., Choi, C. S., & Vivekananda Rao, P. 2016, AJ, 151, 69
Stépień, K. 2004, in Stars as Suns : Activity, Evolution and Planets, ed. A. K. Dupree & A. O. Benz, Vol. 219 (San Fransisco, CA: ASP), 967
Szalai, T., Kiss, L. L., Mészáros, S., Vinkó, J., & Csizmadia, S. 2007, A&A, 465, 943
Tian, X.-m., Zhu, L.-y., & Wang, Z.-h. 2019, PASP, 131, 084203
Tylenda, R., Hajduk, M., Kamiński, T., et al. 2011, A&A, 528, A114
Van Hamme, W., Samec, R. G., Gothard, N. W., et al. 2001, AJ, 122, 3436
Wadhwa, S. S. 2005, Ap&SS, 300, 329
Wadhwa, S. S. 2006, Ap&SS, 301, 195
Wadhwa, S. S., De Horta, A., Filipović, M. D., et al. 2021a, MNRAS, 501, 229
Wadhwa, S. S., De Horta, A. Y., Filipović, M. D., et al. 2021, JApA, 43, 94
Wadhwa, S. S., Tothill, N. F. H., DeHorta, A. Y., & Filipović, M. 2021b, RAA, 21, 235
Webbink, R. F. 1976, ApJ, 209, 829
Woźniak, P. R., Vestrand, W. T., Akerlof, C. W., et al. 2004, AJ, 127, 2436
Yang, Y. 2008, Ap&SS, 314, 151
Yang, Y.-G., & Qian, S.-B. 2015, AJ, 150, 69
Yang, Y. G., Qian, S. B., & Soonthornthum, B. 2012, AJ, 143, 122
Yang, Y. G., Qian, S. B., Zhang, L. Y., Dai, H. F., & Soonthornthum, B. 2013, AJ, 146, 35
Yang, Y.-G., Qian, S.-B., Zhu, L.-Y., He, J.-J., & Yuan, J.-Z. 2005, PASJ, 57, 983
Yu, Y.-X., Li, Q., Huang, H.-P., Hu, K., & Xiang, F.-Y. 2022, NewA, 91, 101695
Zhang, J., Qian, S.-B., & Lyu, B. 2020, PASP, 132, 114201
Zhou, X., Qian, S. B., Zhang, J., et al. 2016, ApJ, 817, 133
Zhu, L.-Y., Zhao, E.-G., & Zhou, X. 2016, RAA, 16, 68
Zola, S., Gazeas, K., Kreiner, J. M., et al. 2010, MNRAS, 408, 464
Zola, S., Rucinski, S. M., Baran, A., et al. 2004, AcA, 54, 299